Circuit QED spectra in the ultrastrong coupling regime: How they differ from cavity QED

Samuel Napoli [1,*] Alberto Mercurio [1,2,3,†] Daniele Lamberto [1] Andrea Zappalà [1]
Omar Di Stefano [1] and Salvatore Savasta [1]
[1] Dipartimento di Scienze Matematiche e Informatiche, Scienze Fisiche e Scienze della Terra, Università di Messina, I-98166 Messina, Italy
[2] Laboratory of Theoretical Physics of Nanosystems (LTPN), Institute of Physics, Ecole Polytechnique Fédérale de Lausanne (EPFL), CH-1015 Lausanne, Switzerland
[3] Center for Quantum Science and Engineering, EPFL, CH-1015 Lausanne, Switzerland

(Received 3 October 2024; accepted 23 May 2025; published 8 July 2025)

Cavity quantum electrodynamics (QED) investigates the interaction between resonator-confined radiation and natural atoms. Similar phenomena can be explored using superconducting artificial atoms coupled to microwave resonators. Here, we examine incoherent and coherent spectra in a circuit QED system consisting of a flux qubit coupled to an LC resonator, considering different coupling configurations to the output transmission line. Although such systems can be effectively described by the quantum Rabi model, we demonstrate that the choice of the coupling between the resonator and the input-output channel can significantly affect the emission properties, particularly in the ultrastrong coupling regime. Specifically, we show that when the resonator is capacitively coupled with the input-output transmission line, the spectral features at zero flux offset can be mapped onto those of the cavity QED model. However, this correspondence breaks down for the mutual inductive coupling case. Extending our analysis to the parity-symmetry broken regime of the flux qubit, we further highlight how capacitive and inductive coupling mechanisms lead to distinct spectral features, emphasizing the necessity of a careful input-output treatment for an accurate description of the emission processes.

DOI: 10.1103/9zl7-31f3

I. INTRODUCTION

Superconducting quantum circuits (SQCs) based on Josephson junctions can behave like artificial atoms. They have made it possible to implement experiments in atomic physics and quantum optics on a chip [1]. In contrast to natural atoms, superconducting artificial atoms can be designed, fabricated, and controlled for various research purposes [2–7]. Furthermore, the interaction between artificial atoms and electromagnetic fields can be controlled and engineered with more freedom [8–11].

Superconducting artificial atoms have been used to demonstrate phenomena that cannot be realized or observed in quantum optics experiments with natural atoms. For instance, single- and two-photon processes can coexist in SQCs [12–14], and the coupling between them and microwave fields can become ultrastrong. The ultrastrong coupling (USC) regime was observed for the first time in circuit QED systems in 2010 [15,16], where normalized coupling strengths of $\eta = 0.10$ to 0.12 were achieved. Within this platform, it is possible to explore the light-matter USC regime with a single two-level system (qubit), instead of considering many atoms or collective excitations [17–24].

The dimensionless parameter $\eta = g/\omega_0$, defined as the cavity-emitter coupling rate divided by the qubit transition frequency (or the resonance frequency of a cavity mode), is used to quantify this coupling regime. Typically, USC effects are expected when $\eta \gtrsim 0.1$. At this threshold, the rotating-wave approximation (RWA), which is valid in the weak and strong coupling regimes, begins to break down [16,17,25–27], enabling novel physical processes.

Potential applications of USC include fast and protected quantum information processing [28–31], quantum nonlinear optics [14,32,33], and the enhancement of various quantum phenomena [34–41]. Recently, experiments in USC circuit QED have demonstrated a number of intriguing effects predicted theoretically [33,42]. For a complete and correct comparison between theory and data, accurate models of circuit QED systems are highly desired. Furthermore, SQCs operating in the USC regime are also exploited for the development of topological quantum systems, with potential applications in topological quantum information processing [43–45].

In many cases, the agreement between experimentally measured circuit QED spectra and theoretical predictions in the USC regime is established by comparing the observed spectral resonances with theoretically calculated transition energies (see, e.g., Refs. [15,22,39]). Furthermore, reflection and transmission spectra in circuit QED are often computed without explicitly incorporating the specific nature of the resonator–waveguide interaction. While the output spectra do not depend significantly on the interaction Hamiltonian de-

*Contact author: samuel.napoli@studenti.unime.it
†Contact author: alberto.mercurio96@gmail.com

scribing the input-output port in the WC and SC regimes, we show that they can be substantially affected by the specific form of this interaction when the qubit-resonator interaction enters the USC regime.

Here, we theoretically investigate a system consisting of a flux qubit coupled to an LC oscillator circuit [22,23,46–50], where both subsystems interact with their respective thermal reservoirs. We compute both coherent and incoherent spectra considering arbitrary light-matter interaction strengths, ranging from the weak to the deep-strong coupling (DSC) regime, where the coupling rate exceeds the bare resonance frequencies [22,46,50,51]. In particular, as in typical experimental settings, we consider the emission process arising from the coupling of the resonator to a coplanar open transmission line (TL), which acts as an input-output port. Two coupling mechanisms are examined: (i) mutual inductive coupling between the resonator and the TL, and (ii) capacitive coupling between the resonator and the TL. Our approach shows that incorporating the specific form of the resonator-TL interaction, through a rigorous input-output analysis and a master equation approach, is essential for accurately describing the emission process in the USC regime, as it can significantly influence the spectral features. Moreover, it has recently been shown that the degree of suppression of the Purcell effect significantly depends on whether the coupling between the resonator and the TL is capacitive or inductive [31].

Within this theoretical framework, we first analyze incoherent emission spectra as a function of the coupling strength and flux offset, under incoherent (thermal-like) excitation of the artificial superconducting atom. We find that at zero flux offset, the spectral properties of the capacitive coupling can be mapped onto those of a typical cavity QED model (e.g., a system with a natural atom), as a consequence of the equivalence between the input-output operators in the two systems, in contrast to the mutual inductive coupling scenario. Subsequently, we study the emission spectra as a function of the flux offset. Finally, we investigate coherent spectra, which are widely used to characterize the spectral properties of circuit QED systems.

II. THEORETICAL FRAMEWORK

In this section, we consider a circuit QED system composed of a flux qubit galvanically coupled to an LC resonator [18,22,46,50]. We also study the coupling of this system, through a mutual inductance M, to an infinite TL [see Fig. 1(a)], then the capacitive coupling of the qubit-LC circuit with a semi-infinite TL [see Fig. 1(b)]. The complete canonical quantization procedure is described in Appendix A.

A. System model

A key feature of the flux qubit is the strong anharmonicity of its energy spectrum, hence permitting a safe *two-level approximation* even in the presence of very high light-matter coupling strengths [50]. Thus, the Hamiltonian of the flux qubit can be easily written in the first two energy states basis ($\{|g\rangle, |e\rangle\}$) as $\hat{\mathcal{H}}_q = \omega_0\,\hat{\sigma}_z/2$ (henceforth $\hbar = 1$), where $\omega_0 = \sqrt{\Delta^2 + \epsilon^2}$. Here, Δ is the tunnel splitting and $\epsilon = 2I_p(\Phi_{\rm ext} - \Phi_0/2)$ is the energy bias between the supercurrents

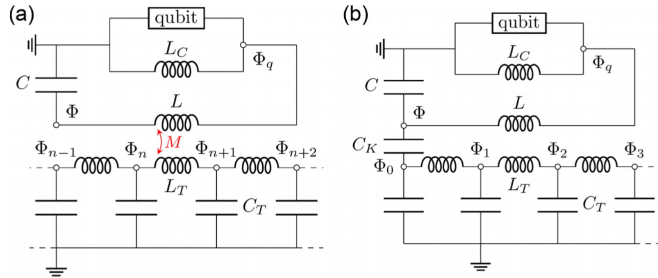

FIG. 1. (a) Circuit diagram of a flux qubit galvanically coupled to the LC resonator. The infinite transmission line interacts with the inductance L of the LC resonator through the mutual inductance M. The dynamical variables are indicated by the nodes. (b) The semi-infinite transmission line is connected to the system through the capacitance C_K.

flowing in opposite directions ($\{|L\rangle, |R\rangle\}$), where I_p is the critical current of the qubit, $\Phi_{\rm ext}$ is the external magnetic flux applied to the superconducting loop, and Φ_0 is the flux quantum [3,22,47,50,52,53]. The node flux $\hat{\Phi}_q$ across the qubit and the coupler L_C can also be projected on the $\{|g\rangle, |e\rangle\}$ basis, giving as a result $\hat{\Phi}_q \simeq I_p L_C\,\hat{\tilde{\sigma}}_x$, where $\cos\theta = \epsilon/\omega_0$, $\sin\theta = \Delta/\omega_0$, and $\hat{\tilde{\sigma}}_x = (\cos\theta\,\hat{\sigma}_z - \sin\theta\,\hat{\sigma}_x)$, note that potential nonlinear terms have been disregarded. Thus, the Hamiltonian $\hat{\mathcal{H}}_0$ of this system, describing the qubit-LC energy and their galvanic interaction, reads as

$$\hat{\mathcal{H}}_0 = \frac{\omega_0}{2}\hat{\sigma}_z + \omega_r \hat{a}^\dagger\hat{a} + \omega_r\,\eta(\hat{a}^\dagger + \hat{a})\hat{\tilde{\sigma}}_x, \tag{1}$$

where $\eta = L_C I_p I_{\rm zpf}/\omega_r$ is the resonator-qubit coupling normalized with respect to the resonance frequency $\omega_r \simeq 1/\sqrt{(L_C + L)C}$ of the LC oscillator, current $I_{\rm zpf}$ and flux $\Phi_{\rm zpf}$ zero-point fluctuations are related so that $I_{\rm zpf} = \Phi_{\rm zpf}/L$. It is worth stressing that whatever variation of the applied flux, which is proportional to ϵ, would modify the resonance frequency of the LC circuit ω_r, $I_{\rm zpf}$, and, as a consequence, the normalized coupling due to the presence of the coupler L_C. However, in this theoretical framework, ω_r and $I_{\rm zpf}$ are assumed to be independent from ϵ. A thorough analysis of this aspect can be found in Refs. [22,42].

B. Input-output relations

In this section, we demonstrate how different coupling schemes with the TL in Fig. 1 lead to distinct input-output relations. We will show that this aspect has consequences in the observed spectral features.

Regarding Fig. 1(a), the total Hamiltonian can be written as

$$\hat{\mathcal{H}}_M = \hat{\mathcal{H}}_0 + \hat{\mathcal{H}}_{\rm tl} + \hat{\mathcal{V}}_M, \tag{2}$$

where $\hat{\mathcal{H}}_0$ is the Hamiltonian of Eq. (1). Moreover, $\hat{\mathcal{H}}_{tl} = \int_0^{+\infty} d\omega\,\omega\,\hat{b}^\dagger_\omega\hat{b}_\omega$, where $\hat{b}_\omega(\hat{b}^\dagger_\omega)$ are the bosonic annihilation (creation) operators for the continuum frequency modes of the TL, satisfying the commutation relation $[\hat{b}_\omega, \hat{b}^\dagger_{\omega'}] = \delta(\omega - \omega')$.

The mutual interaction term results as

$$\hat{\mathcal{V}}_M = i\,\frac{1}{\Phi_{\rm zpf}}\,\hat{\Phi}_L \int_0^{+\infty} d\omega\; g(\omega)\,[\hat{b}_\omega - \hat{b}^\dagger_\omega], \tag{3}$$

where $\hat{\Phi}_L = \hat{\Phi} - \hat{\Phi}_q = \Phi_{\rm zpf}(\hat{a} + \hat{a}^\dagger - 2\eta\,\hat{\sigma}_x)$ and $g(\omega) = \sqrt{\gamma_r\,\omega/(2\pi\omega_r)}$, with $\sqrt{\gamma_r/(2\pi)} = \alpha\,\Phi_{\rm zpf}\,(\Lambda/v_0)\sqrt{\omega_r}$. Here, we denote γ_r as the damping rate of the LC resonator. Furthermore, $\Lambda = \sqrt{Z_0}/4\pi$, Z_0 is the TL impedance, $\alpha = M/L\,l_T$, and $v_0 = 1/\sqrt{l_T\,c_T}$ is the velocity of the light in the TL, $l_T = L_T/\Delta x$ and $c_T = C_T/\Delta x$ are the inductance and the capacitance at each site of the TL per unit of length, and Δx is the distance between two sites.

Figure 1(b) displays the flux qubit-LC-oscillator system capacitively coupled to the TL. We will show that the different coupling mechanisms in Figs. 1(a) and 1(b) can influence the observed spectra, especially when the coupling between the flux qubit and the LC oscillator reaches the USC or DSC regime. The total Hamiltonian is

$$\hat{\mathcal{H}}_C = \hat{\mathcal{H}}_0 + \hat{\mathcal{H}}_{\rm tl} + \hat{\mathcal{V}}_C, \tag{4}$$

where the interaction with the TL reads as

$$\hat{\mathcal{V}}_C = \; i(\hat{a}^\dagger - \hat{a}) \int_0^{+\infty} d\omega\, g(\omega)\, i(\hat{b}^\dagger_\omega - \hat{b}_\omega), \tag{5}$$

where, in this case, $g(\omega) = \sqrt{\gamma_r\,\omega/(2\pi\,\omega_r)}$ and $\sqrt{\gamma_r} = C_K\,\omega_r/\sqrt{v_0 c_T C}$. We observe that the system operator $\hat{X}_C = i(\hat{a}^\dagger - \hat{a})$, appearing in the system-TL interaction Hamiltonian [see Eq. (5)], differs from that in the case of inductive coupling: $\hat{X}_M = \hat{a} + \hat{a}^\dagger - 2\eta\,\hat{\sigma}_x$. This difference, as expected, has a direct impact on the input-output voltage expressions. In Appendix B, we provide the derivation for both cases in detail.

We find that for the mutual inductive coupling

$$\hat{V}^{\pm}_{M_{\rm out}}(x,t) = \hat{V}^{\pm}_{\rm in}(x,t) - \frac{M}{2L}\,\dot{\hat{\Phi}}^{\pm}_L(x,t), \tag{6}$$

and for the capacitive coupling

$$\hat{V}^{\pm}_{C_{\rm out}}(t - x/v_0) = \hat{V}^{\pm}_{\rm in}(t + x/v_0) + Z_0\frac{C_K}{C}\dot{\hat{Q}}^{\pm}(t - x/v_0). \tag{7}$$

Here, the $\pm$ label indicates positive $(+)$ and negative $(-)$ frequency operators.

C. Master equation and emission spectra

In the following, we will numerically diagonalize the closed system Hamiltonian $\hat{\mathcal{H}}_0$ and will treat the interaction of the system with the external reservoirs, including the input-output TL, within a master equation approach suitable for light-matter systems in the USC regime.

Equations (2) and (4) lead to generalized master equations (GMEs), as discussed in Ref. [54]:

$$\dot{\hat{\rho}} = -i[\hat{\mathcal{H}}_0, \hat{\rho}] + \mathcal{L}_g\,\hat{\rho}. \tag{8}$$

The Liouvillian superoperator $\mathcal{L}_g$ involves the operators that are responsible for the interaction of the system with the baths (the complete equation is presented in Appendix C). The TL, schematically displayed in Fig. 1, is one of the system baths. Additional bath channels can, for example, describe qubit spontaneous emission losses and internal losses of the resonator. We also observe that the two different schemes in Figs. 1(a) and 1(b) give rise to different terms in the Liouvillian superoperator (see Appendix C). Regarding the qubit, we assume that the interaction with the relative reservoir occurs through the operator $\hat{\sigma}_x$ for both cases (the same operator in the qubit-LC interaction term). Also, the damping rates of the system are reported in Appendix C.

In Sec. III, we present emission spectra under incoherent (thermal-like) qubit excitation, in the absence of input drive $\langle \hat{V}^{\pm}_{\rm in}\rangle \approx 0$. As a consequence, for the configuration in Fig. 1(a), the voltage measured from the input-output port is determined by the following system operator [see Eq. (6)]:

$$\dot{\hat{\Phi}}_L \propto \dot{\hat{X}}_M = \left[i\,(\hat{a}^\dagger - \hat{a}) - 2\eta\,\frac{\omega_0}{\omega_r}\sin\theta\,\hat{\sigma}_y \right]. \tag{9}$$

For the configuration displayed in Fig. 1(b), the output voltage is determined by [see Eq. (7)]

$$\dot{\hat{Q}} \propto \dot{\hat{X}}_C = -(\hat{a}^\dagger + \hat{a} + 2\,\eta\,\hat{\sigma}_x). \tag{10}$$

Once the density matrix at the steady state $\hat{\rho}_{ss}$ is numerically derived from Eq. (8), and applying the quantum regression theorem [55,56], the power spectrum can be expressed as

$$S_{M(C)}(\omega) \propto {\rm Re}\int_0^{+\infty} d\tau\, e^{-i\omega\tau}\,\langle \dot{\hat{X}}^-_{M(C)}(t+\tau)\dot{\hat{X}}^+_{M(C)}(t)\rangle_{\rm ss}, \tag{11}$$

where, for a generic system operator $\hat{S}$,

$$\hat{S}^+ = \sum_{i,j>i} S^{i,j}\,|i\rangle\langle j|\,, \tag{12}$$

represents the positive frequency component of $\hat{S}$, $\{|i\rangle\}$ are the eigenstates of $\hat{\mathcal{H}}_0$ ordered according to growing energies, and $S^{i,j} = \langle i|\hat{S}|j\rangle$ are the matrix elements. The negative frequency component $\hat{S}^-$ also corresponds to $(\hat{S}^+)^\dagger$. All remaining constant factors deriving from Eqs. (6) and (7) are not considered. Moreover, the time shift between the negative and positive frequency components and the spatial dependence have no impact on the resulting spectra, since we evaluate the power spectra at the steady state. We also analyze the emission properties for the cavity QED model, where a single-mode resonator interacts with a real two-level atom (see Sec. III A). In this case, Eq. (11) has to be specified for the electric field operator in the dipole gauge, replacing $\dot{\hat{X}}_{M(C)}$ with

$$\hat{X}_D = i(\hat{a} - \hat{a}^\dagger) - 2\eta\,\hat{\sigma}_x, \tag{13}$$

see Refs. [56,57] for further details.

In order to inspect how the emission spectra depend on the transition matrix elements of the operators in Eq. (11), it is useful to derive a more explicit form for the emission spectra. Specifically, by applying the quantum regression theorem and numerically diagonalizing the Liouvillian (see Appendix C), we obtain

$$S_{C(M)}(\omega) \simeq -\beta \sum_{l\neq k} \left|\dot{X}^{k,l}_{C(M)}\right|^2 \rho^{k,k}_{\rm ss}\,\frac{\lambda^{(R)}_{k,l}}{\left(\omega - \lambda^{(I)}_{k,l}\right)^2 + \lambda^{2(R)}_{k,l}}. \tag{14}$$

Here, β is a proportional factor, while $\lambda^{(R)}_{l,k}$ and $\lambda^{(I)}_{l,k}$ denote the real and imaginary parts of the Liouvillian eigenvalues, respectively. Thus, Eq. (14) shows that the emission spectrum is a sum of Lorentzian profiles spanning all transitions from the k-th to the l-th eigenfrequency determined by the Hamiltonian in Eq. (1). The amplitude of each peak depends on the squared modulus of the matrix element associated with the specific transition: $|\dot{X}^{k,l}_{C(M)}|^2 = |\langle k|\dot{\hat{X}}_{C(M)}|l\rangle|^2$, as well as a thermal-like population factor $\rho^{k,k}_{\rm ss}$. This relation is also valid for the cavity QED case, substituting $\dot{\hat{X}}_{C(M)}$ with $\hat{X}_D$. More details on the derivation of Eq. (14) and the discussion of the Liouvillian spectrum can be found in Appendix C.

D. Reflection

In this subsection, we outline the method used to compute the coherent (reflection) spectra which will be presented in Sec. IV. The theoretical description of a USC system under coherent drive requires particular care [32]. In this regime, the time dependence of the driving Hamiltonian, involving the operators coupled to the TL [see Eqs. (3) and (5)], cannot be eliminated through a unitary transformation, due to the presence of counter-rotating terms [58]. This limitation prevents the existence of a stationary steady state, resulting in a periodic time-dependent density matrix $\hat{\rho}_{ss}(t)$. The period $T = 2\pi/\omega_d$ only depends on the frequency of the input signal $\omega_d/2\pi$. This behavior aligns with the Floquet formalism, as discussed in Refs. [32,33,42,59]. Consequently, the steady state can be expressed as

$$\hat{\rho}_{ss}(t) = \sum_{k=-\infty}^{+\infty} \hat{\rho}^{(k)} e^{ik\omega_d t},$$

where k is an integer number. By employing this expansion and using the generalized master equation (see Appendix C for details), the different Fourier components of the density matrix can be determined. In particular, when computing the expectation value of a positive-frequency operator, e.g., $\langle \hat{X}^+\rangle$ at the drive frequency ω_d, the $k = -1$ contribution is the only relevant term. For a driving tone in a coherent state, the frequency-dependent reflection S^M_{11} for the mutual inductive coupling can be directly obtained from Eq. (6) (see Appendix C), yielding

$$S^M_{11} = \left|\frac{\langle \hat{V}^+_{M_{\rm out}}\rangle}{\langle \hat{V}^+_{\rm in}\rangle}\right| = \left|1 - \frac{\sqrt{2\pi}}{|b_{\rm in}|}\sqrt{\frac{\omega_d\,\gamma_m}{\omega_r}}\,{\rm Tr}\hat{X}^+_M\,\hat{\rho}^{(-1)}\right|, \tag{15}$$

where $|b_{\rm in}|^2$ represents the photon rate of the coherent drive and γ_m denotes the damping rate of the input-output port. It is important to note that Eq. (15) describes a one-port excitation-detection configuration from the perspective of the circuit QED system (reflection). However, from the standpoint of the TL, this setup can also be interpreted as a two-port scheme, since the signal is detected on the side opposite to the input. In Sec. IV, we compare our spectra with those reported in Refs. [22,46]. Since Ref. [46] treats $\hat{a} + \hat{a}^\dagger$ as the system operator coupled to the input-output port, it is instructive to also evaluate the reflection spectrum using a trace over $(\hat{a} + \hat{a}^\dagger)^+$, rather than $\hat{X}^+_M$ as in our primary analysis. We therefore define

$$\bar{S}_{11} = \left|1 - \frac{\sqrt{2\pi}}{|b_{\rm in}|}\sqrt{\frac{\omega_d\,\gamma_m}{\omega_r}}\,{\rm Tr}[(\hat{a} + \hat{a}^\dagger)^+\hat{\rho}^{(-1)}]\right|. \tag{16}$$

Similarly, starting from Eq. (7), the reflection in the capacitive coupling scheme can be written as

$$S^C_{11} = \left|\frac{\langle \hat{V}^+_{C_{\rm out}}\rangle}{\langle \hat{V}^+_{\rm in}\rangle}\right| = \left|1 + \frac{\sqrt{2\pi}}{|b_{\rm in}|}\sqrt{\frac{\omega_d\,\gamma_c}{\omega_r}}\,{\rm Tr}\hat{X}^+_C\,\hat{\rho}^{(-1)}\right|, \tag{17}$$

where γ_c is the damping rate of the input-output port. A similar method to derive a semi-analytical expression of the coherent spectra, as well as the relationship between the matrix elements of the output operators and the spectral amplitude, can be found in Ref. [42].

III. EMISSION SPECTRA

In this section, we investigate the emission properties of the system under incoherent excitation of the qubit. For simplicity, we assume a zero temperature for the photonic reservoir ($T_r = 0$). Moreover, we consider the following damping rates: $\gamma_q/\Delta = 10 \times \gamma_r/\omega_r = 10^{-2}$, so the system losses originate mainly from the qubit. The incoherent excitation of the qubit is modeled by assuming a qubit reservoir at an effective temperature $T_q/\omega_r \neq 0$ (the Boltzmann constant k_B is set to 1). Numerical simulations are performed with *QuantumToolbox* [60], which is a cutting-edge Julia package designed for quantum physics simulations, closely emulating the popular Python QuTiP package [61,62].

A. Parity symmetry (zero flux offset)

We start analyzing the zero flux offset case ($\epsilon = 0$, implying $\theta = \pi/2$), corresponding to a system described by the standard quantum Rabi model (QRM) Hamiltonian [see Eq. (1)].

We study the nonequilibrium dissipative dynamics of this circuit QED system under incoherent (thermal-like) excitation. In particular, we solve numerically the steady-state master equation, setting the effective temperature of the qubit $T_q/\omega_r = 0.1$. The system's incoherent excitation through the qubit reservoir is able to populate the lowest energy excited states of the system $|\tilde{n}_\pm\rangle$, which in turn decay toward the lower energy states. In the QRM, beyond the strong-coupling regime, the eigenstates do not exhibit the simple structure of the Jaynes-Cummings (JC) model. Therefore, we use a generalized notation for these states by introducing a tilde [56,63]. In particular, the system energy states are labeled so that in the small η limit $|\tilde{n}_\pm\rangle$ coincides with the corresponding JC state $|n_\pm\rangle$.

Figures 2(a) and 2(b) present the resulting emission steady-state spectra as a function of the system coupling rate η. Specifically, Fig. 2(a) shows the case of capacitive coupling with the TL, while Fig. 2(b) displays the spectra obtained for the inductive coupling with the input-output TL. Both panels clearly highlight the transitions $(\tilde{1}_-, \tilde{0})$, $(\tilde{2}_-, \tilde{1}_-)$, and $(\tilde{1}_+, \tilde{0})$ (in ascending order of frequency). As expected, the $(\tilde{1}_-, \tilde{0})$ transition line is the most intense for any values of η at such low effective temperature, being the lowest energy transition. The other transitions tend to become brighter at increasing coupling strength, until the decoupling fate occurs in the DSC limit [51,64]. We observe that the mutual inductive spectra exhibit a quenching of the $(\tilde{1}_+, \tilde{0})$ spectral line when the coupling ranges roughly from 0.4 to 1 [see Fig. 2(b)]. This

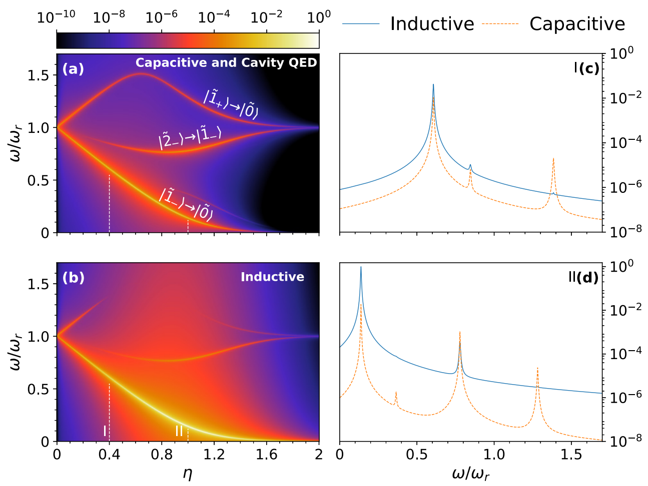

FIG. 2. Logarithmic emission spectra obtained for $T_q/\omega_r = 0.1$, $\Delta/\omega_r = 1$, and $\epsilon = 0$. (a) Logarithmic spectra $S_C(\omega)$ as a function of η at the steady state $\hat{\rho}_{ss}$, for the system capacitively coupled to the TL (also valid for the cavity QED case). (b) Logarithmic spectra for the mutual inductive coupling, $S_M(\omega)$, with the TL. Spectra (a) and (b) are normalized with respect to the absolute maximum value. (c) Logarithmic spectrum computed for $\eta = 0.4$. (d) In this case, the logarithmic spectrum is evaluated at $\eta = 1$. Spectra (c) and (d) are normalized with respect to the maximum value of spectra (a) and (b).

different behavior between the two spectra is determined by the matrix elements of the corresponding system observables coupled to the output channels (see Fig. 3). Figures 2(c) and 2(d) display the spectra obtained fixing specific values of the normalized coupling: $\eta = 0.4,\ 1$, respectively.

Figure 3 shows the squared modulus of the system matrix elements determining the output emission associated to the transitions $|\tilde{1}_-\rangle \rightarrow |\tilde{0}\rangle$ and $|\tilde{1}_+\rangle \rightarrow |\tilde{0}\rangle$, versus the normalized coupling strength η: $|\langle\tilde{1}_-|\dot{\hat{X}}_{M(C)}|\tilde{0}\rangle|^2$ [Fig. 3(a)] and $|\langle\tilde{1}_+|\dot{\hat{X}}_{M(C)}|\tilde{0}\rangle|^2$ [Fig. 3(b)].

These results are clear evidence of how the calculated spectra are influenced by the observable coupled to the output port. This influence, however, becomes evident only in the USC or DSC regime. It is also interesting to compare these findings for circuit QED systems with the corresponding results for a cavity QED model, we consider the atomic transition interacting with the cavity field via standard dipolar coupling [56,57,65–68], and where the photodetection rate is proportional to the expectation value of the product of the negative and positive electric-field operators [69] [see Eq. (13)]. It turns out that the dipolar cavity QED spectra coincide with the circuit QED ones computed for the capacitive coupling to the output TL [see Fig. 2(a)]. This can be understood by observing that, applying a phase rotation $\hat{a} \rightarrow i\hat{a}$ ($\hat{a}^\dagger \rightarrow -i\hat{a}^\dagger$) to the cavity QED Hamiltonian and to the electric-field operator $\hat{X}_D$, the circuit QED Hamiltonian, and the output operator proportional to $\dot{\hat{Q}}$ [see Eq. (10)] are obtained. We can interpret this correspondence, noting that the output capacitive coupling carries the information of the electric field.

In Appendix D, we report additional parity-symmetry spectra at a higher effective temperature T_q.

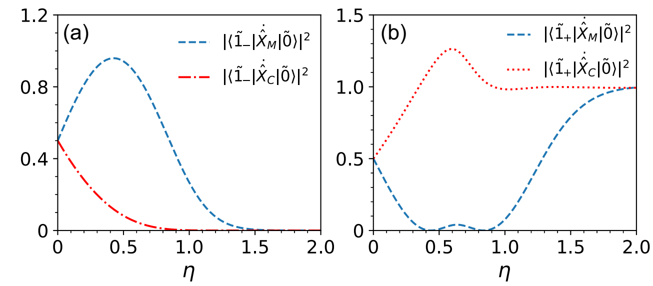

FIG. 3. Squared modulus of two transition matrix elements as a function of η, where $\epsilon = 0$ and $\Delta/\omega_r = 1$. Panel (a) shows $|\langle\tilde{1}_-|\dot{\hat{X}}_{M(C)}|\tilde{0}\rangle|^2$, while panel (b) displays $|\langle\tilde{1}_+|\dot{\hat{X}}_{M(C)}|\tilde{0}\rangle|^2$. As shown in Sec. III A, for $\epsilon = 0$, the operator associated with the electric field in the dipole gauge has the same expression as $\dot{\hat{X}}_C$, up to a phase rotation. Consequently, the matrix elements of $\hat{X}_D$ coincide with those of $\dot{\hat{X}}_C$ (red curves). This observation is crucial in explaining why the emission spectra of the capacitive coupling scheme match those of the cavity QED model in Fig. 2(a).

B. Symmetry breaking (non-zero flux offset)

Circuit QED systems consisting, for example, of an LC oscillator interacting with a flux qubit are usually characterized by detecting spectra as a function of the qubit flux offset ϵ [22,46,50]. For $\epsilon \neq 0$, the parity selection rule of the standard QRM breaks down, and the system can be described by a generalized quantum Rabi model [see Eq. (1)]. In this subsection, we present incoherent emission spectra versus the flux offset ϵ for a normalized coupling strength $\eta = 0.6$. We also consider an effective temperature of the qubit $T_q/\omega_r = 0.15$. Figure 4 displays the evolution (as a function of the flux offset) of several transitions. Note that we have switched the notation

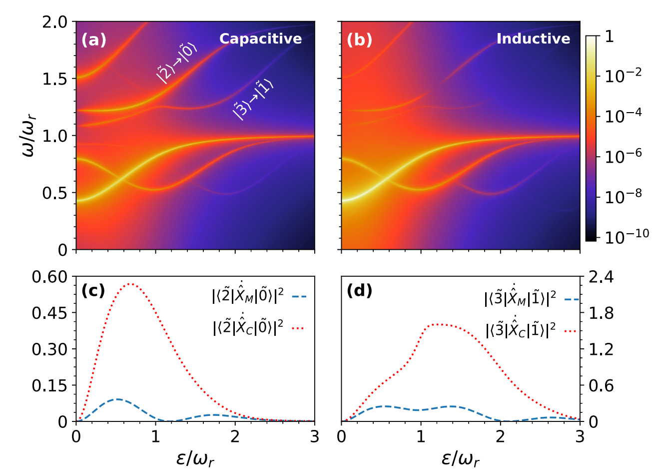

FIG. 4. Logarithmic emission spectra obtained for $T_q/\omega_r = 0.15$, $\Delta/\omega_r = 1$, and $\eta = 0.6$. (a) Logarithmic spectra $S_C(\omega)$ as a function of ϵ/ω_r, for the system capacitively coupled to the TL. (b) Logarithmic spectra for the mutual inductive coupling, $S_M(\omega)$, with the TL. Spectra (a) and (b) are normalized with respect to the absolute maximum value. The specific spectral lines discussed in the text are indicated in panel (a). Panels (c) and (d) report two relevant transition matrix elements of $\dot{\hat{X}}_C$ and $\dot{\hat{X}}_M$ (the transitions displaying differences, see text).

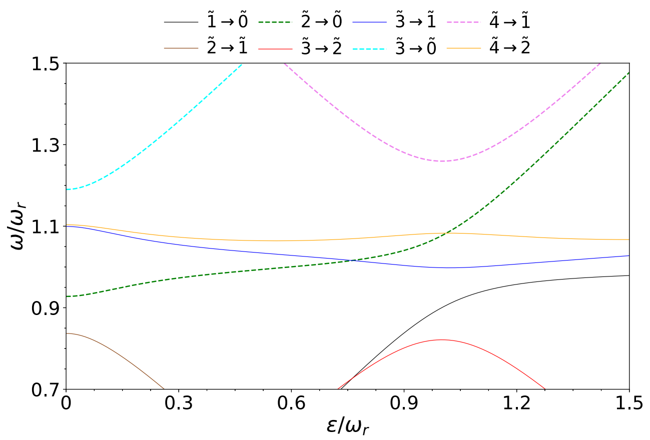

FIG. 5. Energy transitions as a function of ϵ/ω_r for $\eta = 1.01$ and $\Delta/\omega_r = 0.69$. The dotted lines indicate the transitions that exhibit the differences discussed in Sec. IV.

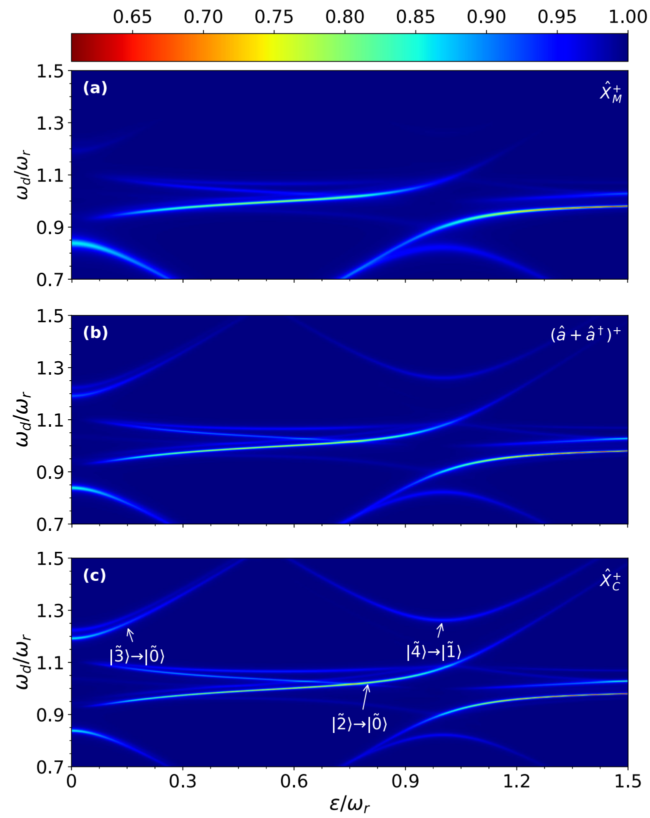

FIG. 6. Coherent spectra obtained for $\eta = 1.01$ and $\Delta/\omega_r = 0.69$. (a) Reflection spectra $S_{11}^M(\omega_d)$, (b) $\bar{S}_{11}(\omega_d)$, and (c) $S_{11}^C(\omega_d)$. The output operator used in each case is indicated in the top-right corner of each panel. Transitions discussed in the main text are explicitly labeled. The colormap is normalized such that the maximum value is 1, and the minimum corresponds to the lowest value across all spectra.

of the energy eigenstates from $|\tilde{n}_\pm\rangle$ to $|\tilde{n}\rangle$, increasing n, the energy grows.

We observe that the lowest transition, $(\tilde{1}, \tilde{0})$, is the most dominant for any ϵ for both of the interaction kinds with the TL.

Figures 4(c) and 4(d) show the squared modulus of the expectation values of the relevant output system operators determining the intensity of two emission lines (associated to the transitions $|\tilde{2}\rangle \to |0\rangle$ and $|\tilde{3}\rangle \to |1\rangle$). As explicitly illustrated in Figs. 4(c) and 4(d), these two transitions are forbidden at $\epsilon = 0$. Moreover, we observe that these matrix elements explain the different intensities of the lines highlighted in Figs. 4(a) and 4(b).

In Appendix D, we investigate emission spectra in the DSC regime and also varying Δ.

IV. COHERENT SPECTRA

In this section, we examine the coherent emission properties of the system. Specifically, we calculate reflection spectra obtained by coupling inductively $[S_{11}^M(\omega_d)]$ and capacitively $[S_{11}^C(\omega_d)]$ the circuit-QED system with an input-output TL, according to the configurations sketched in Fig. 1. For the calculations, we considered parameters which are very similar to those describing 'CIRCUIT III' in Ref. [22]: $\eta = 1.01$ and $\Delta/\omega_r = 0.69$.

In Fig. 5, we plot the transition energies as a function of the normalized flux offset ϵ/ω_r. They determine the main spectral lines in the considered spectral window (see Fig. 6). As expected, the transition energies in Fig. 5 correspond to those observed in Refs. [22,46] (here, the considered spectral range is larger) and will not be discussed further here. Throughout this section, we use the following damping rates: $\gamma_m/\omega_r = \gamma_c/\omega_r = 10^{-3}$ and $\gamma_q/\omega_r = 0.005$. The effective temperatures are all put to 0.55. In order to also excite higher energy levels, $|b_{\rm in}|$ is set to 0.03. All the coherent spectra have been obtained using the generalized Liouvillian described in Appendix C.

Figure 6(a) shows the reflection for the mutual inductive coupling with the TL (S_{11}^M) as a function of ω_d/ω_r and ϵ/ω_r. The transitions $(\tilde{1}, \tilde{0})$, $(\tilde{2}, \tilde{0})$, and $(\tilde{2}, \tilde{1})$ are those with the lowest reflection (the highest reduction of the input signal).

As discussed in Sec. II D, a complete comparison between different models also requires computing $\bar{S}_{11}$. For this reason, we include this case in Fig. 6(b). Moreover, in Fig. 6(c), we display the reflection spectra (S_{11}^C) for the system capacitively coupled to the TL. The main differences between the three panels in Fig. 6 can be associated to the $(\tilde{2}, \tilde{0})$, $(\tilde{3}, \tilde{0})$, and $(\tilde{4}, \tilde{1})$ spectral lines.

The transition $(\tilde{2}, \tilde{0})$ is visible up to $\epsilon/\omega_r = 1.5$ in both $\bar{S}_{11}$ and S_{11}^C spectra, as shown in Fig. 6. However, this spectral line quenches for $\epsilon/\omega_r \geqslant 1.2$ in the S_{11}^M reflection spectra [see Fig. 6(a)].

The $(\tilde{3}, \tilde{0})$ spectral line displays a greater reduction of the input signal (i.e., lower reflection) in Fig. 6(c) compared to Fig. 6(b). Additionally, Fig. 6(a) highlights the highest reflection for this transition among the analyzed cases, with quenching observed for $\epsilon/\omega \geqslant 0.3$. Finally, the $(\tilde{4}, \tilde{1})$ transition is not visible in Fig. 6(a), while it is present in both Figs. 6(b) and 6(c). All the previous observations are supported by the matrix elements shown in Fig. 7. Unfortunately, this spectral region was not reported in Ref. [22]. In summary, the results in Fig. 6 show that the coherent spectra calculated using $\hat{a} + \hat{a}^\dagger$ ($\bar{S}_{11}$) as system operator coupled to the output

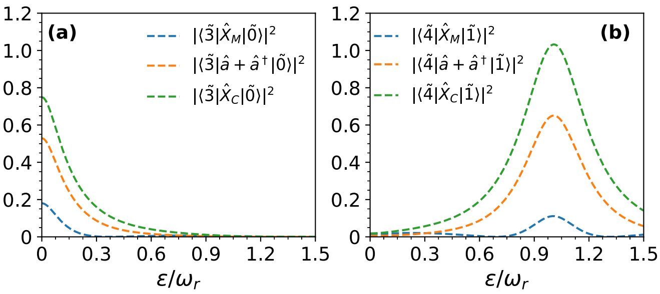

FIG. 7. Squared modulus of three transition matrix elements as a function of ϵ/ω_r, with $\eta = 1.01$ and $\Delta/\omega_r = 0.69$. Panel (a) shows $|\langle\tilde{3}|\hat{X}_{M(C)}|\tilde{0}\rangle|^2$ and $|\langle\tilde{3}|(\hat{a}+\hat{a}^\dagger)|\tilde{0}\rangle|^2$, while panel (b) reports $|\langle\tilde{4}|\hat{X}_{M(C)}|\tilde{1}\rangle|^2$ and $|\langle\tilde{4}|(\hat{a}+\hat{a}^\dagger)|\tilde{1}\rangle|^2$.

port can differ significantly from those associated with $\hat{X}_M$ (S_{11}^M), which accounts for the inductive coupling between the resonator and the TL.

V. CONCLUSIONS

We presented a general framework for calculating spectra in circuit QED systems, which is also suitable for those operating in the USC and DSC regimes. We applied it to calculate emission spectra in a system constituted by a flux qubit coupled to an LC electromagnetic resonator, under incoherent (thermal-like) excitation of the qubit. We find that, even at zero flux offset, when the energy levels correspond to those of the quantum Rabi model for dipolar atomic emitters (cavity QED), the circuit QED spectra may significantly differ from the corresponding cavity QED ones. In particular, we show that the circuit QED spectra can depend on how the resonator is coupled to the output port used for detection. In the case of a resonator capacitively coupled to the output port, cavity QED spectra are recovered in the absence of qubit flux offset.

We also computed reflection spectra under coherent drive. In this case as well, the spectra can depend on how the system is coupled to the input-output TL. These differences between circuit and cavity QED spectra, even at zero flux offset, originate from different light-*matter* coupling Hamiltonian (or Lagrangian) terms. In cavity QED, the interaction Lagrangian term is of the form coordinate-momentum (field coordinate-matter momentum in the Coulomb gauge and conversely in the dipole gauge), see, e.g., Ref. [34]. In contrast, in the circuit QED systems here considered, the corresponding interaction term is of the form coordinate-coordinate (or momentum-momentum in the so-called charge gauge [52]).

These results indicate that an accurate description of both incoherent and coherent spectra in the USC and DSC regimes requires taking into account the proper system variable which is probed. An interesting extension of the theoretical approach adopted in this work would be its application to a multiqubit system described by the generalized Dicke model [39,70,71]. Indeed, the ability to engineer the relative phases of qubit-resonator couplings (see, e.g., Ref. [39]) and to control the single-qubit flux offsets enables the realization of highly tunable circuital configurations. This would enhance the differences in spectral features between these circuital schemes, mostly in the USC and DSC regimes. This topic will be the object of future studies. This framework can also be applied to study quantum nonlinear optics processes in ultrastrong circuit QED [33,39,42]. Very recently, it has been shown that spontaneous Raman scattering of incident radiation can be observed in USC cavity QED systems without external enhancement or coupling to any vibrational degree of freedom [32]. Raman scattering processes can be evidenced as resonances in the emission spectrum, which become visible as the cavity-QED system approaches the USC regime. It would be interesting to calculate the corresponding Raman spectra in circuit QED, which is an ideal platform to observe these effects.

ACKNOWLEDGMENTS

S.S. acknowledges support by the Army Research Office (ARO) through Grant No. W911NF1910065. We also acknowledge discussions with Fabio Mauceri.

APPENDIX A: CIRCUIT QUANTIZATION

In this Appendix, we present the Lagrangian and the Hamiltonian of the circuital system considered throughout this work (see Fig. 1). Such a circuit is subsequently coupled to TLs operating as input-output ports.

We consider a single flux qubit whose Lagrangian $\mathcal{L}_q$ is given by [3]

$$\mathcal{L}_q = 1/2\, C_j \dot{\Phi}_q^2 - \Phi_q^2/2\tilde{L} + E_j \cos[2\pi/\Phi_0\,(\Phi_q - \Phi_{\rm ext})],$$

where $\tilde{L} \simeq (L L_C)/(L + L_C)$ is the equivalent inductance which does not take into account the contribution of the loop inductance L_j.

Considering that $C_K \ll \{C_T, C\}$, the total Lagrangian (consisting of the circuit QED system coupled capacitively to the input-output TL) is given by

$$\mathcal{L}_C = \mathcal{L}_q + \frac{1}{L}\Phi\Phi_q + \frac{1}{2}\underline{\dot{\Phi}}^T\,\underline{\underline{C}}\,\underline{\dot{\Phi}} - \frac{\Phi^2}{2L} - \frac{(\Phi_1 - \Phi_0)^2}{2L_T} + \sum_{i=1}^{\infty}\frac{C_T}{2}\dot{\Phi}_i^{\,2} - \sum_{i=1}^{\infty}\frac{(\Phi_{i+1} - \Phi_i)^2}{2L_T}, \tag{A1}$$

where

$$\underline{\dot{\Phi}} = \begin{pmatrix}\dot{\Phi}\\ \dot{\Phi}_0\end{pmatrix}, \quad \underline{\underline{C}} = \begin{pmatrix} C + C_K & -C_K \\ -C_K & C_T + C_K\end{pmatrix}. \tag{A2}$$

From Eq. (A1), it is possible to obtain the total Hamiltonian:

$$\mathcal{H}_C = \mathcal{H}_0 + \mathcal{H}_{\rm tl} + \frac{C_K}{C C_T} Q\, Q_0, \tag{A3}$$

where

$$\mathcal{H}_0 = \mathcal{H}_q + \mathcal{H}_{\rm LC} + \mathcal{H}_g,$$

is the flux gauge Hamiltonian, including, respectively, the qubit Hamiltonian [50]

$$\mathcal{H}_q = \frac{Q_q^2}{2C_j} + \frac{\Phi_q^2}{2\tilde{L}} - E_j \cos\left[\frac{2\,\pi}{\Phi_0}(\Phi_q - \Phi_{\rm ext})\right], \tag{A4}$$

the LC oscillator term

$$\mathcal{H}_{LC} = \frac{Q^2}{2C} + \frac{\Phi^2}{2L}, \tag{A5}$$

and the coordinate-coordinate (galvanic) interaction term

$$\mathcal{H}_g = -\frac{1}{L}\Phi\Phi_q.$$

Moreover, the Hamiltonian of the TL is given by

$$\mathcal{H}_{\rm tl} = \frac{1}{2C_T}Q_0^2 + \frac{(\Phi_1-\Phi_0)^2}{2L_T} + \sum_{i=1}^{\infty}\frac{Q_i^2}{2C_T} + \sum_{i=1}^{\infty}\frac{(\Phi_{i+1}-\Phi_i)^2}{2L_T}.$$

We take the continuum limit of the TL and, as a consequence, need to introduce the continuous quantities $\phi(x)$ for the flux field and $\rho_c(x) = Q_n/\Delta x$ for a charge density field [4]. The canonical quantization can be performed by promoting the canonical variables to operators, that is $[\hat{\Phi}, \hat{Q}] = i$, $[\hat{\Phi}_q, \hat{Q}_q] = i$, and $[\hat{\phi}(x), \hat{\rho}_c(x')] = i\,\delta(x-x')$.

We now consider a semi-infinite TL, which acts as an input-output port. In this particular case, we can expand the charge field operator as (see, e.g., Ref. [18])

$$\hat{\rho}_c(x) = i\int_0^{\infty} d\omega\sqrt{\frac{\omega\, c_T}{\pi\, v_0}}\,\cos\left(\frac{\omega x}{v_0}\right)(\hat{b}_\omega^\dagger - \hat{b}_\omega). \tag{A6}$$

In the LC circuit, the charge operator can be expressed as

$$\hat{Q} = iQ_{\rm zpf}\,(\hat{a}^\dagger - \hat{a}), \tag{A7}$$

where $Q_{\rm zpf} = \sqrt{(C\omega_r)/2}$. Thus, by substituting Eqs. (A7) and (A6) in the last term of Eq. (A3), we recover Eqs. (4) and (5) in the continuum limit of the TL.

Analogously to the capacitive case, we can obtain the full Hamiltonian for the mutual inductive coupling between the circuit and the TL [see Fig. 1(a)]. The total Hamiltonian (consisting of the circuit QED system coupled inductively to the input-output TL) reads

$$\begin{aligned}\mathcal{H}_M = {}& \mathcal{H}_q + \frac{Q^2}{2\,C} + \frac{1}{2\,\tilde{L}}\,\Phi^2 + \frac{1}{2\,L}(\Phi-\Phi_q)^2 + \frac{1}{2\,C_T}\\ &\times\sum_{j=1} Q_j^2 + \frac{1}{2\tilde{L}_T}(\Phi_{n+1}-\Phi_n)^2 + \frac{1}{2\,L_T}\\ &\times\sum_{j\neq n}(\Phi_{j+1}-\Phi_j)^2 + \frac{\Phi-\Phi_q}{\tilde{M}}\,(\Phi_{n+1}-\Phi_n).\end{aligned} \tag{A8}$$

Note that from the last term in the last row of Eq. (A8), we can argue how the coupling with the TL is obtained through an effective mutual inductance $\tilde{M} = (L\,L_T - M^2)/M$ (Ref. [9]). Furthermore, note that we have introduced in Eq. (A8) the rescaled inductances $\tilde{L} = (L\,L_T - M^2)/L_T$ and $\tilde{L}_T = (L\,L_T - M^2)/L$.

Considering the infinite extension of the TL, performing the continuum limit and the quantization procedure, the flux field $\hat{\phi}(x)$ operator can be expanded as [4]

$$\hat{\phi}(x) = \int_0^{+\infty} d\omega\,\frac{\Lambda}{\sqrt{\omega}}(\hat{b}_\omega\,e^{ikx} + \hat{b}_\omega^\dagger\,e^{-ikx}), \tag{A9}$$

where $k = \omega/v_0$ is the wave number. The interaction Hamiltonian between the system and the TL, $\hat{\mathcal{V}}_M$, can be expressed as

$$\hat{\mathcal{V}}_M = \alpha\,\hat{\Phi}_L\int_{-\infty}^{\infty} dx\,\delta(x)\frac{\partial\hat{\phi}(x)}{\partial x}, \tag{A10}$$

where

$$\hat{\Phi}_L = \hat{\Phi} - \hat{\Phi}_q = \Phi_{\rm zpf}\,[\hat{a} + \hat{a}^\dagger - 2\eta\,(\cos\theta\,\hat{\sigma}_z - \sin\theta\,\hat{\sigma}_x)].$$

In the end, we find

$$\hat{\mathcal{V}}_M = i\,\frac{1}{\Phi_{\rm zpf}}\,\hat{\Phi}_L\int_0^{+\infty} d\omega\,\alpha\,\Phi_{\rm zpf}\,\frac{\Lambda}{v_0}\,\sqrt{\omega}\,[\hat{b}_\omega - \hat{b}_\omega^\dagger], \tag{A11}$$

so Eqs. (2) and (3) are demonstrated.

APPENDIX B: INPUT-OUTPUT THEORY

In this Appendix, we derive the input-output relations in order to establish which system operator is related to the voltage measured for both coupling schemes.

In the case of the infinite TL connected to the qubit-LC system through a mutual inductance, we find that the continuum limit of the Hamiltonian of Eq. (A8) reads as

$$\hat{\mathcal{H}}_M = \hat{\mathcal{H}}_0 + \int_{-\infty}^{+\infty} dx\left(\frac{\hat{\rho}_c^2(x)}{2c_T} + \frac{(\partial_x\hat{\phi})^2}{2l_T}\right) + \frac{M}{Ll_T}\,\hat{\Phi}_L\int_{-\infty}^{+\infty} dx\,\delta(x)\partial_x\hat{\phi}. \tag{B1}$$

Therefore, the resulting Heisenberg equations of motion are

$$\dot{\hat{\phi}}(x) = \frac{\hat{\rho}(x)}{c_T}\,, \tag{B2}$$

and

$$\begin{aligned}\dot{\hat{\rho}}(x) &= \int_{-\infty}^{+\infty} dx'\left\{\frac{i}{l_T}\partial_{x'}\hat{\phi}[\partial_{x'}\hat{\phi}, \hat{\rho}(x)] + \frac{iM}{Ll_T}\delta(x')[\partial_{x'}\hat{\phi}, \hat{\rho}(x)]\right\}\\ &= -\int_{-\infty}^{+\infty} dx'\,\frac{1}{l_T}(\partial_{x'}\hat{\phi})\,\partial_{x'}\delta(x'-x) - \int_{-\infty}^{+\infty} dx'\,\frac{M}{L\,l_T}\delta(x')\partial_{x'}\delta(x'-x)\hat{\Phi}_L\\ &= \frac{1}{l_T}\big(\partial_x^2\hat{\phi}\big) + \frac{M}{Ll_T}\delta'(x)\hat{\Phi}_L.\end{aligned} \tag{B3}$$

Substituting this last equation in Eq. (B2), we obtain

$$\ddot{\hat{\phi}}(x) = \frac{\dot{\hat{\rho}}(x)}{c_T} = v_0^2\big(\partial_x^2\hat{\Phi}\big) + \frac{M}{c_T\,Ll_T}\delta'(x)\hat{\Phi}_L, \tag{B4}$$

corresponding in the Fourier space to

$$\big(k^2 + \partial_x^2\big)\hat{\phi}(x,\omega) = -\frac{M}{v_0^2\,c_T Ll_T}\,\hat{\Phi}_L(\omega)\delta'(x). \tag{B5}$$

The solution to this differential equation can be expressed by means of the Green's functions [72]:

$$\hat{\phi}^{\pm}_{M_{\rm out}}(x,\omega) = \hat{\phi}^{\pm}_{\rm in}(x,\omega) - \left(\frac{M}{2v_0^2 l_T Lc_T}e^{\pm i\,k|x|}\,\hat{\Phi}^{\pm}_L(\omega)\right). \tag{B6}$$

Thus, since $\hat{V}^{\pm}_{M_{\rm out}} = \dot{\hat{\phi}}^{\pm}_{M_{\rm out}}$, we obtain the output voltage as

$$\hat{V}^{\pm}_{M_{\rm out}}(x,\omega) = \hat{V}^{\pm}_{\rm in}(x,\omega) \pm i\omega \frac{M}{2L} e^{\pm ik|x|}\, \hat{\Phi}^{\pm}_{L}(\omega). \tag{B7}$$

The last equation can be written in the time domain as

$$\hat{V}^{\pm}_{M_{\rm out}}(x,t) = \hat{V}^{\pm}_{\rm in}(x,t) - \frac{M}{2L}\, \dot{\hat{\Phi}}^{\pm}_{L}(x,t), \tag{B8}$$

where

$$\hat{\Phi}^{\pm}_{L}(x,t) = \int_0^{\infty} d\omega\, e^{\pm i(\omega/v_0)|x|}\, \hat{\Phi}^{\pm}_{L}(\omega) e^{\mp i\omega t}. \tag{B9}$$

For the capacitive coupling with the semi-infinite TL, following the quantum network theory and imposing the boundary condition at $x = 0$ [4,55,73], the resulting output voltage can be written as

$$\hat{V}^{\pm}_{C_{\rm out}}(t - x/v_0) = \hat{V}^{\pm}_{\rm in}(t + x/v_0) + Z_0 \frac{C_K}{C} \dot{\hat{Q}}^{\pm}(t - x/v_0). \tag{B10}$$

APPENDIX C: GENERALIZED LIOUVILLIAN, EMISSION SPECTRUM, AND REFLECTION FORMULAS

In this Appendix, we explicitly present the full form of the generalized Liouvillian used in Eq. (8). Following the derivation in Ref. [54], we obtain

$$\begin{aligned}\mathcal{L}_g\,\hat{\rho} = \frac{1}{2} \sum_{i=(r,q)(\omega,\omega')>0} \Bigg\{ &\frac{\gamma_i\,\omega'}{\omega_i}\, n_{\rm th}(\omega',T_i)[\hat{A}^-_i(\omega')\hat{\rho}(t)\hat{A}^+_i(\omega) - \hat{A}^+_i(\omega)\hat{A}^-_i(\omega')\hat{\rho}(t)] + \frac{\gamma_i\,\omega}{\omega_i}\, n_{\rm th}(\omega,T_i) \\ &\times [\hat{A}^-_i(\omega')\hat{\rho}(t)\hat{A}^+_i(\omega) - \hat{\rho}(t)\hat{A}^+_i(\omega)\hat{A}^-_i(\omega')] + \frac{\gamma_i\,\omega}{\omega_i}[n_{\rm th}(\omega,T_i)+1][\hat{A}^+_i(\omega)\hat{\rho}(t)\hat{A}^-_i(\omega') \\ &- \hat{A}^-_i(\omega')\hat{A}^+_i(\omega)\hat{\rho}(t)] + \frac{\gamma_i\,\omega'}{\omega_i}\,[n_{\rm th}(\omega',T_i)+1][\hat{A}^+_i(\omega)\hat{\rho}(t)\hat{A}^-_i(\omega') - \hat{\rho}(t)\hat{A}^-_i(\omega')\hat{A}^+_i(\omega)]\Bigg\} \\ &+ \frac{\gamma_q}{2\Delta}\, T_q\, \mathcal{D}\big[\hat{\tilde{\sigma}}^{(0)}_x\big]\hat{\rho}(t) + \frac{\gamma_q}{2\Delta}\,(T_q+1)\,\mathcal{D}\big[\hat{\tilde{\sigma}}^{(0)}_x\big]\hat{\rho}(t),\end{aligned} \tag{C1}$$

where $n_{\rm th}(\omega,T_i) = (e^{\omega}/T_i - 1)^{-1}$ describes the mean number of thermal photons and ω (or ω') is used for the transition frequencies of the light-matter system. $\hat{A}^{+(-)}_i$ denotes the positive (or negative) frequency component of the corresponding operator written in the diagonal basis of $\hat{\mathcal{H}}_0$ [see Eq. (1)]. Using the following relation for the diagonal terms of a generic system operator

$$\hat{S}^{(0)} = \sum_i S^{i,i}\,|i\rangle\langle i|, \tag{C2}$$

the last row of Eq. (C1) can be shown to describe the pure dephasing effects associated to the zero-frequency component of $\hat{\tilde{\sigma}}_x$, where

$$\mathcal{D}\big[\hat{\tilde{\sigma}}^{(0)}_x\big]\hat{\rho} = \hat{\tilde{\sigma}}^{(0)}_x\hat{\rho}\,\hat{\tilde{\sigma}}^{(0)}_x - \tfrac{1}{2}\hat{\tilde{\sigma}}^{(0)}_x\hat{\tilde{\sigma}}^{(0)}_x\,\hat{\rho} - \tfrac{1}{2}\,\hat{\rho}\,\hat{\tilde{\sigma}}^{(0)}_x\,\hat{\tilde{\sigma}}^{(0)}_x, \tag{C3}$$

is the Lindblad dissipator. If the parity symmetry of the flux qubit is not broken ($\epsilon = 0$), this term goes to zero. In Eq. (C1), for $i = r$, ω_i corresponds to the LC resonance frequency ω_r, whereas, for $i = q$, ω_i is associated with Δ. Moreover, the operator $\hat{A}_r$ corresponds to $\hat{X}_C$, $\hat{X}_M$, or $\hat{X}_D$ in the case of the capacitive coupling, inductive coupling, or cavity QED, respectively. Regarding the qubit internal losses, $\hat{A}_q = \hat{\tilde{\sigma}}_x$ for both circuit schemes, and γ_q represents the damping rate for this loss channel, whereas $\hat{A}_q = \hat{\sigma}_x$ when we consider the cavity QED dissipation (see Secs. II B and II C).

In the interaction picture, the terms in the first six rows of Eq. (C1) oscillate at frequencies $\pm(\omega - \omega')$. As shown in Ref. [54], if such a difference is much greater than the damping rates, these highly oscillating terms can be neglected. Their numerical computation can give rise to singularities in the logarithmic spectra, which can be prevented by the introduction of a Gaussian numerical filter:

$$F(\omega,\omega') = e^{-\frac{|\omega-\omega'|^2}{2b^2}}. \tag{C4}$$

The generalized master equation can be reconnected to the dressed master equation found in Ref. [63] for very low values of b. The GME works adequately for quantum optical systems displaying hybrid harmonic-anharmonic energy spectra and for whatever coupling strength regime, even if the Lindblad form is lost at $T \neq 0$.

We now derive the semi-analytical formula for the power spectrum expressed in Eq. (14). By applying the quantum regression theorem [55,74], the correlation function in Eq. (11) at steady state, i.e., in the limit $t \to \infty$, can be expressed as

$$\langle \hat{X}^-(\tau)\hat{X}^+(0)\rangle_{\rm ss},$$

where we introduced a generic system operator $\hat{X}$. Notice that this derivation is general and needs to be explicitly specified according to the corresponding output operator that is considered [see Sec. II C]. Thus, the power spectrum of Eq. (11) can be written as

$$\begin{aligned}S(\omega) &\propto {\rm Re}\int_0^{\infty} d\tau\, e^{-i\omega\tau}\langle \hat{X}^-(\tau)\hat{X}^+(0)\rangle_{\rm ss} \\ &\propto {\rm Re}\int_0^{\infty} d\tau\, e^{-i\omega\tau}{\rm Tr}\hat{X}^- e^{\mathcal{L}_g\tau}[\hat{R}(0)],\end{aligned} \tag{C5}$$

where we have traced out the bath degrees of freedom and employed the quantum regression theorem. To apply the time evolution generated by the Liouvillian, it is convenient to expand $\hat{R}(0) = \hat{X}^+\hat{\rho}^{\rm ss}$ (where $\hat{\rho}^{\rm ss}$ is the steady-state density matrix), which can be interpreted as an initial pseudostate, in a basis of $\mathcal{L}_g$ eigenmatrices [75]. Here, we denote by $\hat{\rho}_n$ the right eigenmatrices of $\mathcal{L}_g$ and by $\hat{\mu}_n$ the left ones:

$$\mathcal{L}_g \, \hat{\rho}_n = \lambda_n \, \hat{\rho}_n, \tag{C6}$$

$$\hat{\mu}_n \mathcal{L}_g = \hat{\mu}_n \, \lambda_n. \tag{C7}$$

The notation in Eq. (C7) indicates that we sorted the eigenvalues and eigenmatrices so that the n-th left eigenvalue coincides with the corresponding right one. Moreover, $\lambda_0 = 0$ and $\hat{\rho}_0$ corresponds to $\hat{\rho}^{\text{ss}}$. At $t = 0$, we expand $\hat{R}(0) = \sum_n c_n \hat{\rho}_n$, thus

$$\hat{R}(\tau) = e^{\mathcal{L}_g \tau} \hat{R}(0) = c_0 \hat{\rho}_0 + \sum_n c_n \, e^{\lambda_n \tau} \, \hat{\rho}_n.$$

As a consequence, Eq. (C5) becomes

$$S(\omega) \propto \text{Re}\left[\sum_{n>0} c_n \text{Tr} \hat{X}^- \hat{\rho}_n \int_0^\infty d\tau \, e^{-(i\omega + \lambda_n)\tau}\right], \tag{C8}$$

and by evaluating the time integral, the power spectrum is finally given by

$$S(\omega) \propto \sum_{n>0} c_n \text{Tr} \hat{X}^- \hat{\rho}_n \frac{-\lambda_n^{(R)}}{\left(\omega - \lambda_n^{(I)}\right)^2 + \lambda_n^{2(R)}}, \tag{C9}$$

where $\lambda_n^{(R)} < 0$ represents the real part of the n-th Liouvillian eigenvalue, while $\lambda_n^{(I)}$ denotes its imaginary part. Examining Eq. (C9), the emission spectrum can be interpreted as a sum of Lorentzian profiles centered at various $\lambda_n^{(I)}$, with widths associated with $\lambda_n^{(R)}$. The steady-state contribution ($\lambda_0 = 0$) is excluded because it would result in a Dirac delta at $\omega = 0$. The expansion coefficients c_n are given by

$$c_n = \text{Tr} \hat{\mu}_n \hat{R} = \text{Tr} \hat{\mu}_n \hat{X}^+ \hat{\rho}_0.$$

This observation not only validates the convergence of the aforementioned time integral but also confirms the association between the real part of the Liouvillian eigenvalues and the dissipative losses of the light-matter system, up to a dressing factor. Regarding the imaginary parts $\lambda_n^{(I)}$, $N^2 - N$ eigenvalues can be associated to specific transition frequencies determined by $\hat{\mathcal{H}}_0$ [see Eq. (1)], subject to minor shifts resulting from the interaction with the reservoirs. Here, $N = (n_{\text{ph}} \times 2)$ denotes the dimensionality of the light-matter system's Hilbert space, where n_{ph} represents the cutoff dimension of the photonic subspace. Notably, apart from the steady state, the remaining N eigenvalues exhibit zero imaginary part; the corresponding eigenmatrices are diagonal (in the basis that diagonalizes $\hat{\mathcal{H}}_0$) and possess zero trace. Based on these observations, we substitute n with $\{l, k\}$, such that $\lambda_{k,l}^{(I)}$ corresponds to the transition frequency between the l-th and k-th eigenstates of the light-matter system ($\hat{\mathcal{H}}_0$). Similarly, assuming nondegenerate transitions and a weak coupling regime between the light and matter subsystems and their respective baths, it is reasonable to approximate $\hat{\rho}_{k,l} \approx |l\rangle\langle k|$ and $\hat{\mu}_{k,l} \approx |k\rangle\langle l|$ (this holds only if $l \neq k$, hence for eigenmatrices associated to eigenvalues having nonzero imaginary part).

Consequently, Eq. (C9) can be reformulated as

$$S(\omega) \simeq \beta \sum_{l \neq k} \text{Tr}|k\rangle\langle l| \hat{X}^+ \hat{\rho}_0 \text{Tr} \hat{X}^- |l\rangle\langle k| \times \frac{-\lambda_{k,l}^{(R)}}{\left(\omega - \lambda_{k,l}^{(I)}\right)^2 + \left(\lambda_{k,l}^{(R)}\right)^2}, \tag{C10}$$

with β being a proportional factor. Given that $\hat{\rho}_0$ is a thermal steady state, it takes a diagonal form with unit trace. Using Eq. (12), we finally recover Eq. (14):

$$S(\omega) \simeq \beta \sum_{l \neq k} |X^{k,l}|^2 \hat{\rho}_0^{k,k} \frac{-\lambda_{k,l}^{(R)}}{\left(\omega - \lambda_{k,l}^{(I)}\right)^2 + \left(\lambda_{k,l}^{(R)}\right)^2}, \tag{C11}$$

where $\hat{\rho}_0^{k,k} = \langle k|\hat{\rho}_0|k\rangle$ and $|X^{k,l}|^2 = |\langle k|\hat{X}|l\rangle|^2$. The emission spectra presented in the main text are calculated by numerically diagonalizing $\mathcal{L}_g$ and vectorizing the operators defined in the Hilbert space of $\hat{\mathcal{H}}_0$.

In Sec. II D, we introduced the reflection formulas. To derive the expressions of S_{11}^M and S_{11}^C, we start from the input-output relations. For the mutual inductive coupling with the TL, the expectation value of the output voltage, considering only its positive-frequency component, is obtained by evaluating Eq. (B8):

$$\left\langle \hat{V}_{M_{\text{out}}}^+ \right\rangle = \langle \hat{V}_{\text{in}}^+ \rangle + \frac{M}{2L}(i\omega_d)\Phi_{\text{zpf}} \langle \hat{X}_M^+ \rangle. \tag{C12}$$

Here, we neglect the spatial dependence of $\hat{V}_{M_{\text{out}}}^+$ since we evaluated the spectra far from the interaction point between the circuit QED system and the TL. Moreover, we assume that $\dot{\hat{X}}_M^+ \approx -i\omega_d \, \hat{X}_M^+$ (steady state). For a coherent-state driving tone, the expectation value of the input voltage is given by

$$\langle V_{\text{in}}^+ \rangle = -i|b_{\text{in}}|\Lambda \sqrt{\omega_d}. \tag{C13}$$

Using the definition of the damping rates $\sqrt{\gamma_r / 2\pi}$ in Eq. (3), we obtain

$$S_{11}^M = \left| \frac{\langle \hat{V}_{M_{\text{out}}}^+ \rangle}{\langle V_{\text{in}}^+ \rangle} \right| = \left| 1 - \frac{\sqrt{2\pi}}{|b_{\text{in}}|} \sqrt{\frac{\omega_d \gamma_m}{\omega_r}} \langle \hat{X}_M^+ \rangle \right|. \tag{C14}$$

Similarly, following the same procedure, we derive the reflection for the capacitive coupling with the TL:

$$S_{11}^C = \left| \frac{\langle \hat{V}_{C_{\text{out}}}^+ \rangle}{\langle V_{\text{in}}^+ \rangle} \right| = \left| 1 + \frac{\sqrt{2\pi}}{|b_{\text{in}}|} \sqrt{\frac{\omega_d \gamma_c}{\omega_r}} \langle \hat{X}_C^+ \rangle \right|. \tag{C15}$$

As discussed in Sec. II D, we employ a master equation approach combined with the Floquet formalism to compute $\langle \hat{X}_M^+ \rangle$ and $\langle \hat{X}_C^+ \rangle$. Differently from the scenario where only incoherent processes occur, the Liouville equation in this case takes the form of

$$\dot{\hat{\rho}} = -i[\hat{\mathcal{H}}_0, \hat{\rho}] + (\mathcal{L}_g + \mathcal{L}_+ e^{i\omega_d t} + \mathcal{L}_- e^{-i\omega_d t})\hat{\rho}, \tag{C16}$$

where $\mathcal{L}_g$ accounts for the system dissipation channels and follows the structure of Eq. (C1). The terms $\mathcal{L}_\pm$ in Eq. (C16) originate from the coherent driving of the system. Specifically,

$$\mathcal{L}_{\pm}\hat{\rho} = \pm i|b_{\rm in}|e^{\pm i\varphi}\sqrt{\frac{\gamma_c\,\omega_d}{2\pi\,\omega_r}}[\hat{X}_C, \hat{\rho}], \tag{C17}$$

$$\mathcal{L}_{\pm}\hat{\rho} = \mp i|b_{\rm in}|e^{\pm i\varphi}\sqrt{\frac{\gamma_m\,\omega_d}{2\pi\,\omega_r}}[\hat{X}_M, \hat{\rho}], \tag{C18}$$

where Eq. (C17) applies to the capacitive coupling case, while Eq. (C18) corresponds to the mutual inductive coupling one. The parameter φ represents the phase of the driving tone. The opposite signs in these equations originate from the nature of the interaction Hamiltonian [see Eqs. (3) and (5)]. By substituting the Fourier expansion of the steady-state density matrix,

$$\hat{\rho}_{ss}(t) = \sum_{k=-\infty}^{+\infty} \hat{\rho}^{(k)} e^{ik\omega_d t}, \tag{C19}$$

into Eq. (C16), we derive the following recursive equation [33]:

$$(\mathcal{L}_g - ik\omega_d)\hat{\rho}^{(k)} + \mathcal{L}_{+}\hat{\rho}^{(k-1)} + \mathcal{L}_{-}\hat{\rho}^{(k+1)} = 0. \tag{C20}$$

The components $\rho^{(k)}$ are numerically computed by solving this equation while truncating the Fourier series at the desired order [33]. The component $k = -1$ is the only significant contribution in the calculation of $\langle \hat{X}_M^{+} \rangle$ and $\langle \hat{X}_C^{+} \rangle$ at the drive frequency, allowing us to recover Eqs. (17) and (15). In Sec. IV, we also numerically compute $\bar{S}_{11}$. In that case, $\hat{a} + \hat{a}^{\dagger}$ replaces $\hat{X}_M$ in Eq. (C14) and in the preceding expressions.

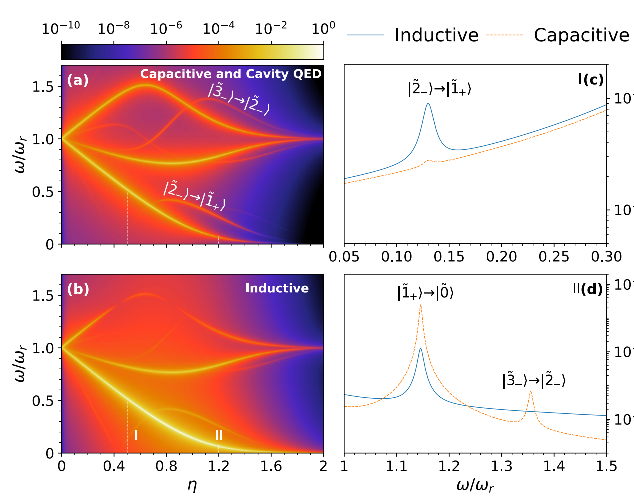

FIG. 8. Logarithmic emission spectra obtained for $T_q/\omega_r = 0.18$, $\Delta/\omega_r = 1$, and $\epsilon = 0$. (a) Logarithmic spectra $S_C(\omega)$ as a function of η, for the system capacitively coupled to the TL (also valid for the cavity QED case). (b) Logarithmic spectra for the mutual inductive coupling, $S_M(\omega)$, with the TL. Spectra (a) and (b) are normalized with respect to the absolute maximum value. (c) Logarithmic spectrum computed for $\eta = 0.5$, the capacitive coupling emission spectrum is enhanced by a factor of 10. (d) In this case, the logarithmic spectrum is evaluated at $\eta = 1.2$. Spectra (c) and (d) are normalized with respect to the maximum value of spectra (a) and (b).

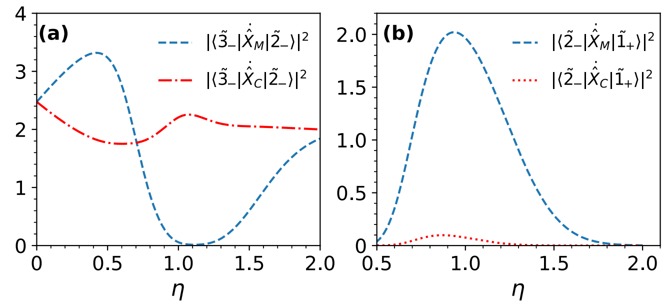

FIG. 9. Squared modulus of two transition matrix elements as a function of η, where $\epsilon = 0$ and $\Delta/\omega_r = 1$. (a) This panel shows $|\langle \tilde{3}_-|\dot{\hat{X}}_{M(C)}|\tilde{2}_-\rangle|^2$, while panel (b) reports $|\langle \tilde{2}_-|\dot{\hat{X}}_{M(C)}|\tilde{1}_+\rangle|^2$.

APPENDIX D: FURTHER SPECTRA

In this Appendix, we extend the treatment discussed in Sec. III. Specifically, we will consider higher excitation strength (T_q) for the parity-symmetry emission spectra. Subsequently, we will calculate emission spectra varying ϵ, with fixed $\Delta = 1$ (as shown in Sec. III B), for higher couplings η in the DSC regime. In the end, further incoherent spectra will be presented for different values of Δ/ω_r.

1. Parity symmetry (zero flux offset)

Here, we present emission spectra obtained using the same parameters considered in Sec. III A with a different effective temperature, $T_q = 0.18$ (see Fig. 8).

In contrast to Fig. 2(b), the $(\tilde{1}_+, \tilde{0})$ spectral line is also visible for coupling strengths ranging from 0.4 to 1 (see Fig. 8) due to the higher qubit effective temperature T_q, considering the mutual inductive spectra. However, when $\dot{\hat{X}}_M$ matrix

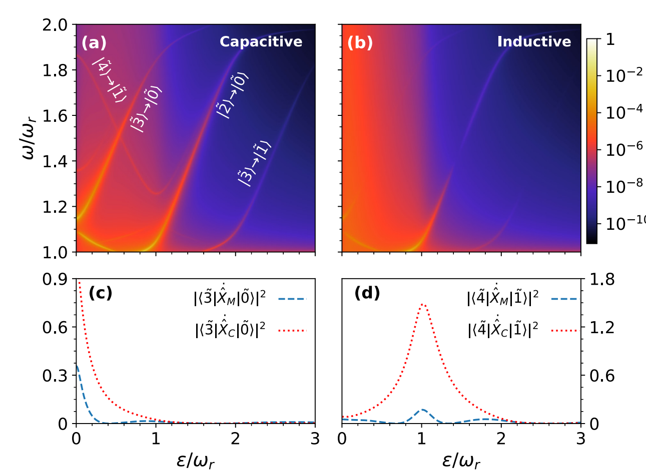

FIG. 10. Logarithmic emission spectra obtained for $T_q/\omega_r = 0.15$, $\Delta/\omega_r = 1$, and $\eta = 1.2$. (a) Logarithmic spectra $S_C(\omega)$ as a function of ϵ/ω_r, for the system capacitively coupled to the TL. (b) Logarithmic spectra for the mutual inductive coupling, $S_M(\omega)$, with the TL. Spectra (a) and (b) are normalized with respect to the absolute maximum value. The specific spectral lines discussed in the text are indicated in panel (a). Panels (c) and (d) report two relevant transition matrix elements of $\dot{\hat{X}}_C$ and $\dot{\hat{X}}_M$ (the transitions displaying differences, see text).

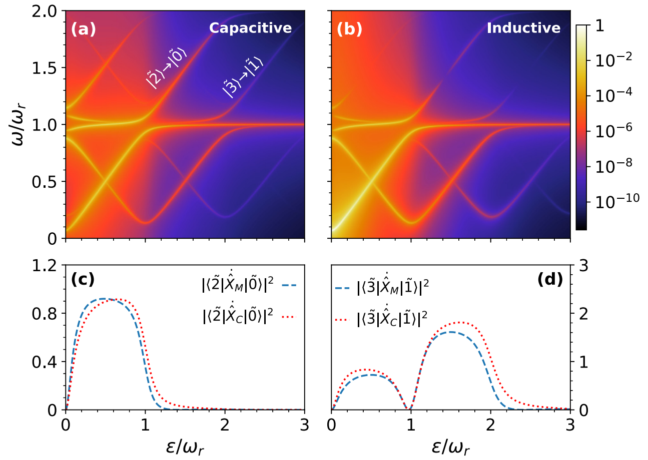

FIG. 11. Logarithmic emission spectra obtained for $T_q/\omega_r = 0.15$, $\Delta/\omega_r = 0.5$, and $\eta = 1$. (a) Logarithmic spectra $S_C(\omega)$ as a function of ϵ/ω_r, for the system capacitively coupled to the TL. (b) Logarithmic spectra for the mutual inductive coupling, $S_M(\omega)$, with the TL. Spectra (a) and (b) are normalized with respect to the absolute maximum value. The specific spectral lines discussed in the text are indicated in panel (a). Panels (c) and (d) report two relevant transition matrix elements of $\dot{\hat{X}}_C$ and $\dot{\hat{X}}_M$.

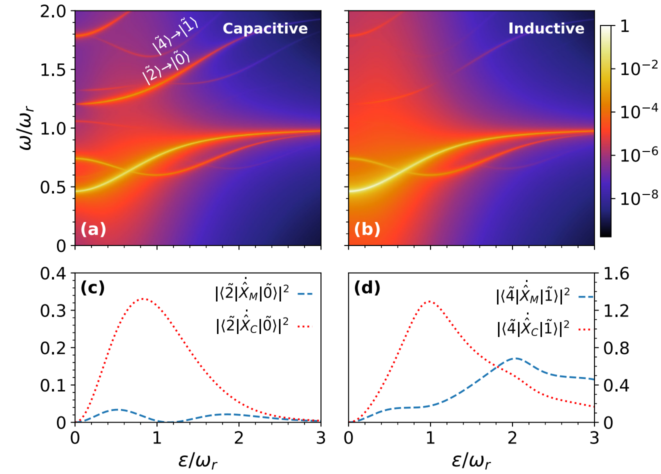

FIG. 12. Logarithmic emission spectra obtained for $T_q/\omega_r = 0.15$, $\Delta/\omega_r = 1.5$, and $\eta = 0.7$. (a) Logarithmic spectra $S_C(\omega)$ as a function of ϵ/ω_r, for the system capacitively coupled to the TL. (b) Logarithmic spectra for the mutual inductive coupling, $S_M(\omega)$, with the TL. Spectra (a) and (b) are normalized with respect to the absolute maximum value. The specific spectral lines discussed in the text are indicated in panel (a). Panels (c) and (d) report two relevant transition matrix elements of $\dot{\hat{X}}_C$ and $\dot{\hat{X}}_M$.

elements vanish for this particular transition [see Fig. 3(b)], we observe a suppression of the mutual inductive power spectra.

Two additional transitions have been highlighted: $(\tilde{2}_-, \tilde{1}_+)$ and $(\tilde{3}_-, \tilde{2}_-)$. When η reaches 0.5, the former is noticeable principally for the mutual inductive spectrum. For $\eta = 1.2$, the transition $(\tilde{3}_-, \tilde{2}_-)$ is present only for the capacitive coupling spectrum [see Figs. 8(c) and 8(d)]. The relative matrix elements of Fig. 9 explain this behavior.

2. Symmetry breaking (nonzero flux offset)

In the following, we present additional emission spectra as a function of the flux offset, considering different values of the normalized coupling strength.

Figure 10 displays results obtained for $\eta = 1.2$. The spectral lines corresponding to the transitions $(\tilde{2}, \tilde{0})$ and $(\tilde{3}, \tilde{1})$ exhibit similar features of Fig. 4. However, the transitions $(\tilde{3}, \tilde{0})$ and $(\tilde{4}, \tilde{1})$ are more visible for the capacitive coupling scheme [see Figs. 10(a) and 10(b)]. Matrix elements for these transitions, which are shown in Figs. 10(c) and 10(d), explain the origin of differences between Figs. 10(a) and 10(b).

3. Varying Δ

Throughout this work, we have used $\Delta/\omega_r = 1$ for all incoherent spectra. Figure 11 is obtained for $\Delta/\omega_r = 0.5$ and $\eta = 1$. In this case, there are still differences between the spectra in Figs. 11(a) and 11(b) observed for particular spectral lines, which are reported in Fig. 11(a), despite the very small differences in the matrix elements [see Figs. 11(c) and 11(d)].

Emission spectra of Figs. 12(a) and 12(b) have been calculated for $\Delta/\omega_r = 1.5$ and $\eta = 0.7$. Also in this case, it is interesting to compare some differences in intensity of particular spectral lines with the corresponding matrix elements in Figs. 12(c) and 12(d).

[1] J. Q. You and F. Nori, Atomic physics and quantum optics using superconducting circuits, Nature (London) **474**, 589 (2011).
[2] J. P. Dowling and G. J. Milburn, Quantum technology: The second quantum revolution, Phil. Trans. R. Soc. B **361**, 1655 (2003).
[3] J. Q. You and F. Nori, Superconducting circuits and quantum information, Phys. Today **58**(11), 42 (2005).
[4] A. Blais, A. L. Grimsmo, S. M. Girvin, and A. Wallraff, Circuit quantum electrodynamics, Rev. Mod. Phys. **93**, 025005 (2021).
[5] U. Vool and M. Devoret, Introduction to quantum electromagnetic circuits, Int. J. Circuit Theory Appl. **45**, 897 (2017).
[6] X. Gu, A. F. Kockum, A. Miranowicz, Y.-X. Liu, and F. Nori, Microwave photonics with superconducting quantum circuits, Phys. Rep. **718–719**, 1 (2017).
[7] L. Frunzio, A. Wallraff, D. Schuster, J. Majer, and R. Schoelkopf, Fabrication and characterization of superconducting circuit QED devices for quantum computation, IEEE Trans. Appl. Supercond. **15**, 860 (2005).
[8] Y. Makhlin, G. Schön, and A. Shnirman, Quantum-state engineering with Josephson-junction devices, Rev. Mod. Phys. **73**, 357 (2001).
[9] P. Krantz, M. Kjaergaard, F. Yan, T. P. Orlando, S. Gustavsson, and W. D. Oliver, A quantum Engineer's guide to superconducting qubits, Appl. Phys. Rev. **6**, 021318 (2019).
[10] A. Blais, S. M. Girvin, and W. D. Oliver, Quantum information processing and quantum optics with circuit quantum electrodynamics, Nat. Phys. **16**, 247 (2020).

[11] M. Devoret, S. Girvin, and R. Schoelkopf, Circuit-QED: How strong can the coupling between a Josephson junction atom and a transmission line resonator be? Annalen der Physik **519**, 767 (2007).

[12] P. Adhikari, M. Hafezi, and J. M. Taylor, Nonlinear optics quantum computing with circuit QED, Phys. Rev. Lett. **110**, 060503 (2013).

[13] F. Deppe, M. Mariantoni, E. P. Menzel, A. Marx, S. Saito, K. Kakuyanagi, H. Tanaka, T. Meno, K. Semba, H. Takayanagi, E. Solano, and R. Gross, Two-photon probe of the Jaynes–Cummings model and controlled symmetry breaking in circuit QED, Nat. Phys. **4**, 686 (2008).

[14] A. F. Kockum, A. Miranowicz, V. Macrì, S. Savasta, and F. Nori, Deterministic quantum nonlinear optics with single atoms and virtual photons, Phys. Rev. A **95**, 063849 (2017).

[15] T. Niemczyk, F. Deppe, H. Huebl, E. Menzel, F. Hocke, M. Schwarz, J. Garcia-Ripoll, D. Zueco, T. Hümmer, E. Solano *et al.*, Circuit quantum electrodynamics in the ultrastrong-coupling regime, Nat. Phys. **6**, 772 (2010).

[16] P. Forn-Díaz, J. Lisenfeld, D. Marcos, J. J. García-Ripoll, E. Solano, C. J. P. M. Harmans, and J. E. Mooij, Observation of the Bloch-Siegert shift in a qubit-oscillator system in the ultra-strong coupling regime, Phys. Rev. Lett. **105**, 237001 (2010).

[17] A. Frisk Kockum, A. Miranowicz, S. De Liberato, S. Savasta, and F. Nori, Ultrastrong coupling between light and matter, Nat. Rev. Phys. **1**, 19 (2019).

[18] P. Forn-Díaz, L. Lamata, E. Rico, J. Kono, and E. Solano, Ultrastrong coupling regimes of light-matter interaction, Rev. Mod. Phys. **91**, 025005 (2019).

[19] W. Qin, A. F. Kockum, C. S. Muñoz, A. Miranowicz, and F. Nori, Quantum amplification and simulation of strong and ultrastrong coupling of light and matter, Phys. Rep. **1078**, 1 (2024).

[20] P. Forn-Díaz, J. J. García-Ripoll, B. Peropadre, J.-L. Orgiazzi, M. A. Yurtalan, R. Belyansky, C. M. Wilson, and A. Lupascu, Ultrastrong coupling of a single artificial atom to an electromagnetic continuum in the nonperturbative regime, Nat. Phys. **13**, 39 (2017).

[21] A. Bayer, M. Pozimski, S. Schambeck, D. Schuh, R. Huber, D. Bougeard, and C. Lange, Terahertz light–matter interaction beyond unity coupling strength, Nano Lett. **17**, 6340 (2017).

[22] F. Yoshihara, T. Fuse, S. Ashhab, K. Kakuyanagi, S. Saito, and K. Semba, Superconducting qubit–oscillator circuit beyond the ultrastrong-coupling regime, Nat. Phys. **13**, 44 (2017).

[23] Z. Chen, Y. Wang, T. Li, L. Tian, Y. Qiu, K. Inomata, F. Yoshihara, S. Han, F. Nori, J. S. Tsai, and J. Q. You, Single-photon-driven high-order sideband transitions in an ultrastrongly coupled circuit-quantum-electrodynamics system, Phys. Rev. A **96**, 012325 (2017).

[24] S. Gambino, M. Mazzeo, A. Genco, O. Di Stefano, S. Savasta, S. Patanè, D. Ballarini, F. Mangione, G. Lerario, D. Sanvitto, and G. Gigli, Exploring light–matter interaction phenomena under ultrastrong coupling regime, ACS Photonics **1**, 1042 (2014).

[25] P. Forn-Díaz, G. Romero, C. J. P. M. Harmans, E. Solano, and J. E. Mooij, Broken selection rule in the quantum Rabi model, Sci. Rep. **6**, 26720 (2016).

[26] D. D. Bernardis, A. Mercurio, and S. D. Liberato, Tutorial on nonperturbative cavity quantum electrodynamics: Is the Jaynes-Cummings model still relevant? J. Opt. Soc. Am. B **41**, C206 (2024).

[27] A. Le Boité, Theoretical methods for ultrastrong light–matter interactions, Adv. Quantum Technol. **3**, 1900140 (2020).

[28] R. Stassi, M. Cirio, and F. Nori, Scalable quantum computer with superconducting circuits in the ultrastrong coupling regime, npj Quantum Inf. **6**, 67 (2020).

[29] Y.-H. Chen, W. Qin, R. Stassi, X. Wang, and F. Nori, Fast binomial-code holonomic quantum computation with ultrastrong light-matter coupling, Phys. Rev. Res. **3**, 033275 (2021).

[30] R. Stassi and F. Nori, Long-lasting quantum memories: Extending the coherence time of superconducting artificial atoms in the ultrastrong-coupling regime, Phys. Rev. A **97**, 033823 (2018).

[31] P. D. Kurilovich, T. Connolly, C. G. L. Bøttcher, D. K. Weiss, S. Hazra, V. R. Joshi, A. Z. Ding, H. Nho, S. Diamond, V. D. Kurilovich, W. Dai, V. Fatemi, L. Frunzio, L. I. Glazman, and M. H. Devoret, High-frequency readout free from transmon multi-excitation resonances, arXiv:2501.09161.

[32] V. Macrì, A. Mercurio, F. Nori, S. Savasta, and C. Sánchez Muñoz, Spontaneous scattering of raman photons from cavity-QED systems in the ultrastrong coupling regime, Phys. Rev. Lett. **129**, 273602 (2022).

[33] S.-P. Wang, A. Mercurio, A. Ridolfo, Y. Wang, M. Chen, T. Li, F. Nori, S. Savasta, and J. Q. You, Strong coupling between a single photon and aphoton pair, arXiv:2401.02738 [quant-ph].

[34] A. Mercurio, S. Abo, F. Mauceri, E. Russo, V. Macrì, A. Miranowicz, S. Savasta, and O. Di Stefano, Pure dephasing of light-matter systems in the ultrastrong and deep-strong coupling regimes, Phys. Rev. Lett. **130**, 123601 (2023).

[35] R. Stassi, A. Ridolfo, O. Di Stefano, M. J. Hartmann, and S. Savasta, Spontaneous conversion from virtual to real photons in the ultrastrong-coupling regime, Phys. Rev. Lett. **110**, 243601 (2013).

[36] S. De Liberato, C. Ciuti, and I. Carusotto, Quantum vacuum radiation spectra from a semiconductor microcavity with a time-modulated vacuum Rabi frequency, Phys. Rev. Lett. **98**, 103602 (2007).

[37] L. Garziano, V. Macrì, R. Stassi, O. Di Stefano, F. Nori, and S. Savasta, One photon can simultaneously excite two or more atoms, Phys. Rev. Lett. **117**, 043601 (2016).

[38] L. Giannelli, E. Paladino, M. Grajcar, G. S. Paraoanu, and G. Falci, Detecting virtual photons in ultrastrongly coupled superconducting quantum circuits, Phys. Rev. Res. **6**, 013008 (2024).

[39] A. Tomonaga, R. Stassi, H. Mukai, F. Nori, F. Yoshihara, and J.-S. Tsai, One photon simultaneously excites two atoms in a ultrastrongly coupled light-matter system, arXiv:2307.15437 [quant-ph].

[40] M.-S. Choi, Exotic quantum states of circuit quantum electrodynamics in the ultra-strong coupling regime, Adv. Quantum Technol. **3**, 2000085 (2020).

[41] A. Ridolfo, M. Leib, S. Savasta, and M. J. Hartmann, Photon blockade in the ultrastrong coupling regime, Phys. Rev. Lett. **109**, 193602 (2012).

[42] S.-P. Wang, A. Ridolfo, T. Li, S. Savasta, F. Nori, Y. Nakamura, and J. Q. You, Probing the symmetry breaking of a light–matter system by an ancillary qubit, Nat. Commun. **14**, 4397 (2023).

[43] F. P. M. Méndez-Córdoba, J. J. Mendoza-Arenas, F. J. Gómez-Ruiz, F. J. Rodríguez, C. Tejedor, and L. Quiroga, Rényi entropy singularities as signatures of topological criticality in coupled photon-fermion systems, Phys. Rev. Res. **2**, 043264 (2020).

[44] F. P. M. Méndez-Córdoba, F. J. Rodríguez, C. Tejedor, and L. Quiroga, From edge to bulk: Cavity-induced displacement

of topological nonlocal qubits, Phys. Rev. B **107**, 125104 (2023).

[45] H.-L. Huang, M. Narożniak, F. Liang, Y. Zhao, J. Clark, M. Gong, Y. Wu, S. Wang, J. Lin, Y. Xu, H. Deng, H. Rong, J. P. Dowling, C.-Z. Peng, T. Byrnes, X. Zhu, and J.-W. Pan, Emulating quantum teleportation of a Majorana zero mode qubit, Phys. Rev. Lett. **126**, 090502 (2021).

[46] F. Yoshihara, T. Fuse, S. Ashhab, K. Kakuyanagi, S. Saito, and K. Semba, Characteristic spectra of circuit quantum electrodynamics systems from the ultrastrong- to the deep-strong-coupling regime, Phys. Rev. A **95**, 053824 (2017).

[47] I. Chiorescu, P. Bertet, K. Semba, Y. Nakamura, C. J. P. M. Harmans, and J. E. Mooij, Coherent dynamics of a flux qubit coupled to a harmonic oscillator, Nature (London) **431**, 159 (2004).

[48] F. Yan, S. Gustavsson, A. Kamal, J. Birenbaum, A. P. Sears, D. Hover, T. J. Gudmundsen, D. Rosenberg, G. Samach, S. Weber, J. L. Yoder, T. P. Orlando, J. Clarke, A. J. Kerman, and W. D. Oliver, The flux qubit revisited to enhance coherence and reproducibility, Nat. Commun. **7**, 12964 (2016).

[49] S. Saito, T. Meno, M. Ueda, H. Tanaka, K. Semba, and H. Takayanagi, Parametric control of a superconducting flux qubit, Phys. Rev. Lett. **96**, 107001 (2006).

[50] F. Yoshihara, S. Ashhab, T. Fuse, M. Bamba, and K. Semba, Hamiltonian of a flux qubit-LC oscillator circuit in the deep–strong-coupling regime, Sci. Rep. **12**, 6764 (2022).

[51] S. De Liberato, Light-matter decoupling in the deep strong coupling regime: The breakdown of the Purcell effect, Phys. Rev. Lett. **112**, 016401 (2014).

[52] V. E. Manucharyan, A. Baksic, and C. Ciuti, Resilience of the quantum Rabi model in circuit QED, J. Phys. A: Math. Theor. **50**, 294001 (2017).

[53] S. Savasta, O. Di Stefano, A. Settineri, D. Zueco, S. Hughes, and F. Nori, Gauge principle and gauge invariance in two-level systems, Phys. Rev. A **103**, 053703 (2021).

[54] A. Settineri, V. Macrí, A. Ridolfo, O. Di Stefano, A. F. Kockum, F. Nori, and S. Savasta, Dissipation and thermal noise in hybrid quantum systems in the ultrastrong-coupling regime, Phys. Rev. A **98**, 053834 (2018).

[55] C. Gardiner and P. Zoller, *Quantum Noise: A Handbook of Markovian and Non-Markovian Quantum Stochastic Methods with Applications to Quantum Optics* (Springer Science & Business Media, Berlin, 2004).

[56] A. Mercurio, V. Macrì, C. Gustin, S. Hughes, S. Savasta, and F. Nori, Regimes of cavity QED under incoherent excitation: From weak to deep strong coupling, Phys. Rev. Res. **4**, 023048 (2022).

[57] A. Settineri, O. Di Stefano, D. Zueco, S. Hughes, S. Savasta, and F. Nori, Gauge freedom, quantum measurements, and time-dependent interactions in cavity QED, Phys. Rev. Res. **3**, 023079 (2021).

[58] C. Sánchez Muñoz, A. Frisk Kockum, A. Miranowicz, and F. Nori, Simulating ultrastrong-coupling processes breaking parity conservation in Jaynes-Cummings systems, Phys. Rev. A **102**, 033716 (2020).

[59] W. Salmon, C. Gustin, A. Settineri, O. D. Stefano, D. Zueco, S. Savasta, F. Nori, and S. Hughes, Gauge-independent emission spectra and quantum correlations in the ultrastrong coupling regime of open system cavity-QED, Nanophotonics **11**, 1573 (2022).

[60] A. Mercurio, Y.-T. Huang, L.-X. Cai, Y.-N. Chen, V. Savona, and F. Nori, QuantumToolbox. jl: An efficient Julia framework for simulating open quantum systems, arXiv:2504.21440.

[61] J. Johansson, P. Nation, and F. Nori, QuTiP: An open-source Python framework for the dynamics of open quantum systems, Comput. Phys. Commun. **183**, 1760 (2012).

[62] J. Johansson, P. Nation, and F. Nori, QuTiP 2: A Python framework for the dynamics of open quantum systems, Comput. Phys. Commun. **184**, 1234 (2013).

[63] F. Beaudoin, J. M. Gambetta, and A. Blais, Dissipation and ultrastrong coupling in circuit QED, Phys. Rev. A **84**, 043832 (2011).

[64] M. Salado-Mejía, R. Román-Ancheyta, F. Soto-Eguibar, and H. M. Moya-Cessa, Spectroscopy and critical quantum thermometry in the ultrastrong coupling regime, Quantum Sci. Technol. **6**, 025010 (2021).

[65] M. Babiker, R. Loudon, and G. W. Series, Derivation of the Power-Zienau-Woolley Hamiltonian in quantum electrodynamics by gauge transformation, Proc. R. Soc. London. A. Math. Phys. Sci. **385**, 439 (1983).

[66] C. Cohen-Tannoudji, J. Dupont-Roc, and G. Grynberg, *Photons and Atoms: Introduction to Quantum Electrodynamics* (Wiley-VCH, New York, 1997).

[67] O. Di Stefano, A. Settineri, V. Macrì, L. Garziano, R. Stassi, S. Savasta, and F. Nori, Resolution of gauge ambiguities in ultrastrong-coupling cavity quantum electrodynamics, Nat. Phys. **15**, 803 (2019).

[68] C. Gustin, S. Franke, and S. Hughes, Gauge-invariant theory of truncated quantum light-matter interactions in arbitrary media, Phys. Rev. A **107**, 013722 (2023).

[69] R. J. Glauber, The quantum theory of optical coherence, Phys. Rev. **130**, 2529 (1963).

[70] L. Garziano, A. Settineri, O. Di Stefano, S. Savasta, and F. Nori, Gauge invariance of the Dicke and Hopfield models, Phys. Rev. A **102**, 023718 (2020).

[71] D. Lamberto, O. Di Stefano, S. Hughes, F. Nori, and S. Savasta, Quantum phase transitions in many-dipole light-matter systems, Phys. Rev. Res. **7**, 013271 (2025).

[72] E. N. Economou, *Green's Functions in Quantum Physics* (Springer Science & Business Media, 2006), Vol. 7.

[73] B. Yurke and J. S. Denker, Quantum network theory, Phys. Rev. A **29**, 1419 (1984).

[74] H.-P. Breuer and F. Petruccione, *The Theory of Open Quantum Systems* (Oxford University Press, Oxford, 2002).

[75] F. Minganti, A. Biella, N. Bartolo, and C. Ciuti, Spectral theory of Liouvillians for dissipative phase transitions, Phys. Rev. A **98**, 042118 (2018).